Catal Lett (2007) 117:1–17
DOI 10.1007/s10562-007-9194-6

Fischer–Tropsch Synthesis: Morphology, Phase Transformation and Particle Size Growth of Nano-scale Particles

Amitava Sarkar · Deepyaman Seth · Alan K. Dozier · James K. Neathery · Hussein H. Hamdeh · Burtron H. Davis

Received: 26 April 2007 / Accepted: 29 June 2007 / Published online: 20 July 2007

Abstract An unpromoted ultrafine iron nano-particle catalyst was used for Fischer–Tropsch synthesis (FTS) in a CSTR at 270 °C, 175 psig, $H_2/CO = 0.7$, and a syngas space velocity of 3.0 sl/h/g Fe. Prior to FTS, the catalyst was activated in CO for 24 h which converted the initial hematite into a mixture of 85% χ-Fe_5C_2 and 15% magnetite, as found by Mössbauer measurement. The activated catalyst results in an initial high conversion (ca. 85%) of CO and H_2; however the conversions decreased to ca. 10% over about 400 h of synthesis time and after that remained nearly constant up to 600 h. Mössbauer and EELS measurement revealed that the catalyst deactivation was accompanied by gradual in situ re-oxidation of the catalyst from initial nearly pure χ-Fe_5C_2 phase to pure magnetite after 400 h of synthesis time. Experimental data indicates that the nucleation for carbide/oxide transformation may initiates at the center of the particle by water produced during FTS. Small amount of ε'-$Fe_{2.2}C$ phase was detected in some catalyst samples collected after 480 h of FTS which are believed to be generated by syngas during FTS. Particle size distribution (PSD) measurements indicate nano-scale growth of individual catalyst particle. Statistical average diameters were found to increase by a factor of 4 over 600 h of FTS. Large particles with the largest dimension larger than 150 nm were also observed. Chemical compositions of the larger particles were always found to be pure single crystal magnetite as revealed by EELS analysis. Small number of ultrafine carbide particles was identified in the catalyst samples collected during later period of FTS. The results suggest that carbide/oxide transformation and nano-scale growth of particles continues either in succession or at least simultaneously; but definitely not in the reverse order (in that case some larger carbide particles would have observed). EELS-STEM measurement reveals amorphous carbon rim of thickness 3–5 nm around some particles after activation and during FTS. Well ordered graphitic carbon layers on larger single crystal magnetite particles were found by EELS-STEM measurement. However the maximum thickness of the carbon (amorphous or graphitic) rim does not grow above 10 nm suggesting that the growths of particles are not due to carbon deposition.

Keywords Fischer-Tropsch synthesis · Iron catalyst · Phase transformation · Iron carbide · Amorphous carbon · Graphitic carbon · Nano-scale growth · Particle size distribution

A. Sarkar · J. K. Neathery · B. H. Davis (✉)
Center for Applied Energy Research, University of Kentucky, 2540 Research Park Drive, Lexington, KY 40511-8479, USA
e-mail: davis@caer.uky.edu

D. Seth
Department of Chemical Engineering, University of Waterloo, Waterloo, ON, Canada N2L 3G1

A. K. Dozier
Chemical and Materials Engineering Department, University of Kentucky Electron Microscopy Center, A004 ASTeCC Building 0286, Lexington, KY 40506, USA

H. H. Hamdeh
Physics Department, Wichita State University, Wichita, KS 67260, USA

1 Introduction

Conversion of syngas ($CO + H_2$) to liquid fuels and chemicals has enormous potential for utilization of the large world reserves of natural gas and coal [1]. Increasingly stringent environmental regulations push the drive for

"clean-fuels" (low-sulfur, low-aromatics); and concerns about the depletion of fossil-fuel reserves make Fischer–Tropsch synthesis (FTS) an environmental-friendly and economically promising route for production of middle-distillate fuels, petroleum blending-stock, a wide variety of hydrocarbons and oxygenates from either coal or natural-gas or biomass-derived syngas [2].

Iron-based catalysts are preferred for FTS utilizing synthesis gas derived from coal or biomass because of their excellent activity for the water gas shift reaction which allows using a synthesis gas with a low H_2/CO ratio (e.g., 0.7) directly without an upstream shift-step. The use of iron-based catalysts is also attractive in view of their lower cost, lower methane selectivity, high olefin-selectivity, lower sensitivity towards poisons and flexible product slate. However, because of the non-selective nature of the FTS, a large amount of waxy material (heavy hydrocarbons) is produced when the catalyst and reactor operation favors long chain growth. This wax can be refined and processed (via hydrocracking, oligomerization, alkylation, etc.) to produce premium quality fuels and chemical feed-stock. During the removal of wax, the catalyst particles must remain suspended in the liquid-phase of the FTS reactor to maintain the required conversion and to avoid catalyst loss. Catalyst/wax separation is also necessary from the standpoint of wax upgrading, since the catalyst fines may foul the catalyst in subsequent wax processing and can degrade the final product quality. As a requirement of the downstream wax processing, the solid content of the slurry-phase FT wax should be limited to below 2–5 ppm [3].

The application of slurry bubble column reactor (SBCR) for liquid phase FTS is advantageous because of excellent control of highly exothermic reaction heat in large-scale industrial operation. Nevertheless the use of iron catalysts in the most economical SBCR has been limited by their high rate of attrition to ultrafine particles leading to catalyst loss, high slurry viscosity and difficulty in wax/catalyst separation.

Phase-transformation of iron catalyst during activation/FTS plays an important role in determining the structural integrity or attrition resistance of the catalyst particles. Sequential phase-modification during the activation process (with CO or synthesis gas) from hematite to magnetite and finally to iron carbides have been reported [4, 5]. Results of previous studies have shown that the formation of surface carbides is required before the catalyst can exhibit high activity [4–7]. The chemical conversion of iron oxides to iron carbides induce a volumetric change because of significant difference in the skeletal densities of carbide and oxide structures (e.g., 7.7 g/cm^3 for Fe_3C as compared to 5.2 g/cm^3 for Fe_3O_4). The volumetric change can cause stress in the particle which may lead attrition and formation of small crystallites of iron carbides that split off rapidly to form ultrafine particles [6, 8, 9]. Physical attrition can also result from collision between catalyst particles and the reactor internals. However, it has been shown that the conversion of iron oxides to iron carbide is dynamic and reversible depending upon the environment [4]. Under oxidizing conditions (e.g., at high water and CO_2 partial pressures), Fe_3O_4 can form, ultimately producing nearly pure Fe_3O_4 particles. It has also been reported that conversion of Fe_3C to Fe_3O_4 results in an increase in volume of 91%, and a similar increase for χ-Fe_5C_2 [10]. Thus the reoxidation step also has the potential to provide severe stress in the individual particle and in the agglomerate to cause the formation of fine particles during FTS operation.

During activation and FTS, the gas composition in contact with the catalyst has the potential to exhibit either reducing or oxidizing properties. A variety of iron carbide/oxide phase may be evolved during the activation/synthesis process. Thus there exists a strong possibility that the catalyst particles may undergo either fragmentation or growth in size depending on the process condition. However, only Kuo et al. [11] have reported so far a tremendous increase in apparent particle size during the slurry-phase FTS which is contrary to what generally observed/reported in literature [6, 9, 12]. The particle size of most of the catalyst used for attrition studies available in the literature are in the micron range. It has been reported that spray dried and calcined iron-based catalyst (Fe/Cu/K/SiO_2) particles in the 30–50 μm range, disintegrated to 1–3 μm size range during 24 h stirring in CSTR under inert gas as well as under FTS conditions [13]. The observed extent of attrition with Fe catalysts is the result of both chemical attrition due to phase transformation and to physical attrition through collisions. In view of the above, it is important to examine the existence of any limiting size of the iron-based catalyst particles under typical FTS process condition. If, when carbidization/FTS is started with larger size particles, attrition and fragmentation results in the formation of particles in a "limiting size range", then the same "limiting size range" should result by growth of smaller particles when the initial particle size (i.e., before carburization/FTS) is in submicron range (e.g., nanoparticles). The use of submicron particles is particularly advantageous for efficient control and utilization of highly exothermic heat of reaction and enhanced mass transfer rate of gaseous reactants to the solid catalysts surface in a SBCR operation [14]. A detailed knowledge of the change of particle size of the submicron particles is therefore needed for design and operation of SBCR and for a mechanical liquid/solid separation system.

The objective of the present study is to monitor the particle size distribution (PSD), morphological and chemical transformation of ultrafine iron nano-catalyst particles (with initial diameters of 3–5 nm) during the carbidization/

FTS in a CSTR using HRTEM, HAADF-STEM, EELS and Mössbauer spectroscopy. The information on the change of PSD can be utilized for design and optimization of a continuous flow filtration unit for wax/catalyst separation.

2 Experimental

2.1 Materials

A commercial ultrafine iron oxide catalyst (NANOCAT® Superfine Iron Oxide, Mach I, Inc.) was used for these experiments. The properties reported for the average particle size of the catalyst was 3–5 nm, surface area of 250 m^2/g, and bulk density of 0.05 g/cm^3. Polywax 850 (polyethylene fraction with average molecular weight of 850), purchased from Baker Petrolite, Inc., was used as the start-up solvent.

2.2 Methods

The FTS experiments were conducted in a 1 L CSTR equipped with a magnetically driven stirrer with turbine impeller, a gas-inlet line, and a vapor outlet line with a SS fritted filter (2 micron) placed external to the reactor. A tube fitted with a SS fritted filter (0.5 micron opening) extends below the liquid level of the reactor for withdrawing reactor wax maintains a nearly constant liquid level in the reactor. Another SS dip-tube (1/8″ OD) extends to the bottom of the reactor and was used to withdraw catalyst/wax slurry from the reactor at different synthesis times. Separate mass flow controllers were used to control the flow of hydrogen and carbon monoxide at the desired rate. The gases were premixed in a mixing vessel before entering to the reactor. Carbon monoxide was passed through a vessel containing lead oxide-alumina to remove traces of iron carbonyl. The mixed gases entered the CSTR below the stirrer operated at 750 rpm. The reactor slurry temperature was maintained constant (±1 °C) by a temperature controller.

The as-received ultrafine iron oxide catalyst (54.7 g) was added to melted (150 °C) Polywax 850 (310 g) in the CSTR to produce a slurry that contained about 15 wt% iron oxide. The reactor temperature was then raised to 270 °C at a rate of 1 °C/min. The catalyst was activated using CO at a space velocity of 3.0 sl/h/g Fe at 270°C and 175 psig for 24 h. At the end of activation period, a sample of activated catalyst (Sample S1) was withdrawn via the slurry withdrawal dip-tube of the CSTR. The FTS was then started by adding synthesis gas mixture to the reactor at a space velocity of 3.0 sl/h/g Fe and a H_2/CO ratio of 0.7. The conversions of CO and H_2 were obtained by gas-chromatography analysis (micro-GC equipped with thermal conductivity detectors) of the reactor exit gas mixture. The reaction products were collected in three traps maintained at different temperatures—a hot trap (200 °C), a warm trap (100 °C) and a cold trap (0 °C). The products were separated into different fractions (rewax, wax, oil and aqueous) for quantification. However, the oil and the wax fractions were mixed prior to GC analysis.

Catalyst/rewax slurry was withdrawn at different reaction times via the dip-tube after sufficient purging. The withdrawal schedule is shown in Table 1. In a typical catalyst slurry sampling procedure, about 7–8 g of catalyst slurry was purged and then 2–3 g of catalyst slurry was collected as representative sample in the reactor at that time. To minimize changes in the particle morphology, the Soxhlet extraction procedure to remove the wax-products was avoided. The withdrawn samples were diluted with hot (about 70 °C) ortho-xylene to remove the high molecular weight FT-wax fractions. It was not possible to completely remove the FT-wax from the catalyst particles by this method. However, the remaining wax acts as a protective cover for the air-sensitive catalyst particles. Solution of relatively clean catalyst particles in ortho-xylene were prepared for use in high resolution transmission electron microscopy (HRTEM) measurements. An optimum ratio of ortho-xylene to catalyst slurry was used so that the catalyst particles form a slightly turbid suspension. A drop of the suspension was placed with a syringe onto a lacey carbon film on 200 mesh copper grid. As the ortho-xylene evaporated, the grid was loaded into the microscope for analysis.

The morphology and in-depth analysis of individual particles were obtained using a field emission analytical transmission electron microscope (JEOL JEM-2010F) operated at an accelerating voltage of 200 kV and equipped with a scanning transmission electron microscope (STEM) unit with high-angle annular dark field (HAADF) detector, and a Gatan imaging filter (GIF)/PEELS system. HRTEM images were recorded under optimal focus condition at a typical magnification of 100–500 K. The electron beam had a point-to-point resolution of 0.5 nm. EELS spectra were recorded in TEM imaging mode with an energy resolution from 1 eV (full width at half maximum of zero loss peak) and dispersion rate 0.2 eV/channel. Gatan Digital Micrograph® software was used for image and EELS data recording and processing.

Mössbauer spectra were collected in a transmission mode by a standard constant acceleration spectrometer (MS-1200, Ranger Scientific). A radiation source of 30 mCi ^{57}Co in Rh matrix was used and spectra were obtained using a gas detector. The catalyst samples collected from the CSTR were in the rewax/PW 850 matrix and were in solid phase at room temperature. This solid matrix was mounted in plexiglass compression holders that present a thin aspect to the γ–ray beam. All samples were investigated at room temperature as well as at cryogenic temperatures, typically with a velocity range of ±10 mm/s.

Table 1 Summary of phase identification of iron from Mössbauer spectroscopy analysis

Sample #	FT Synthesis Time, h	Fraction (%) of Fe at 300 K	Fraction (%)of Fe at 20 K
S1	0 (after 24 h CO carbidization)	85 in χ-Fe_5C_2	84 in χ-Fe_5C_2
		15 in spm	16 in Fe_3O_4
S2	28.9	33 in Fe_3O_4	50 in Fe_3O_4
		48 in χ-Fe_5C_2	50 in χ-Fe_5C_2
		19 in spm	
S3	73.2	65 in Fe_3O_4	76 in Fe_3O_4
		18 in χ-Fe_5C_2	22 in χ-Fe_5C_2
		17 in spm	2 in spm
S4	167.7	89 in Fe_3O_4	91 in Fe_3O_4
		11 in spm	6 in χ-Fe_5C_2
			3 in spm
S5	311	93 in Fe_3O_4	96 in Fe_3O_4
		7 in spm	4 in spm
S6	382.8	100 in Fe_3O_4	99 in Fe_3O_4
			1 in paramag
S7	481.6	93 in Fe_3O_4	93 in Fe_3O_4
		7 γ-Fe_2C	5 in ε'-$Fe_{2.2}C$
			2 in paramag
S8	596.8	100 in Fe_3O_4	90 in Fe_3O_4
			4 in ε'-$Fe_{2.2}C$
			6 in paramag

For the low temperature measurements, the samples were placed inside a vibration free closed cycle cryostat (Cryo-Industries of America). The structural analysis of the samples was done by least-squares fitting of the Mössbauer spectra to a summation of hyperfine sextets. The least-square fitting procedure employed user defined functions within the PeakFit program. The parameters for each sextet in the fit consisted of the position, width and height of the first peak, the hyperfine magnetic field, and the quadrupole electric field. These parameters were allowed to vary freely to obtain the best fit of the experimental data. Errors in the determined percent of Fe values are about ±3% for well-resolved spectra; in those that contain several iron oxide and carbide phase the uncertainty increases with the complexity of the spectrum (i.e., depending on the degree of overlapping and the weakness of the signal). However, these complex spectra are obtained during the course of change from a predominantly iron carbide or iron oxide phase and conform to a general trend.

3 Results

3.1 Catalytic Activity and Stability

The initial activity of the ultrafine iron catalyst was found to be high. When FTS was started with the carbided catalyst, the observed conversion level for CO and H_2 was about 85% and 80%, respectively. Since the ultrafine catalyst did not contain any structural promoter, the catalytic activity showed a slow and gradual decrease during a total time-on-stream (TOS) of about 600 h. The TOS in this case has been counted from the starting of FTS using synthesis gas. The variation of conversion levels of syngas, hydrogen and CO, as calculated from gas analysis, against synthesis time is shown in Fig. 1. A total of eight catalyst slurry samples were collected during the experiment—one sample after carbidization and seven samples during FTS. It should be noted that apart from catalyst deactivation during FTS, the withdrawal of the catalyst particles during the experiment also contributes to the decrease in conversion. The ultrafine Fe catalyst used in the present study did not contain any promoter, so the rate of deactivation is expected to be quite high. The combination of above two factors results in CO and H_2 conversion levels of 9.8% and 20.8%, respectively, after 597 h of FTS.

3.2 Phase Composition by Mössbauer Spectroscopy

Mössbauer spectroscopy was used to follow the dynamic phase transformation between iron oxide and iron carbide during carbidization and FTS. Representative Mössbauer spectra for sample S1, S2, S5, and S8 are shown in Fig. 2a–d, respectively. All of the Mössbauer spectra in the present study represented a complex pattern comprising magnetite, carbide and paramagnetic components. The extent of the

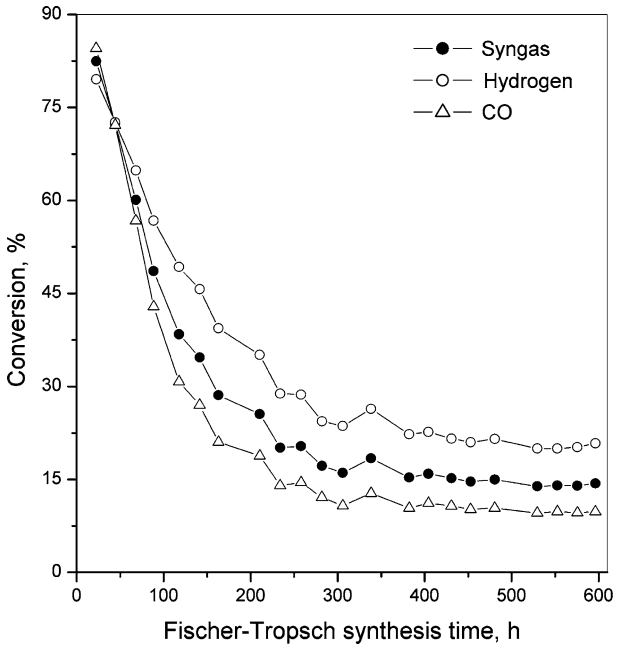

Fig. 1 Conversion of syngas, hydrogen and CO against time-on-stream. Conversion of syngas is calculated as the arithmetic average of hydrogen and CO conversions. FTS effected at 270 °C, 175 psig, $H_2/CO = 0.7$, and a syngas space velocity of 3.0 sl/h/g Fe

resulting magnetic hyperfine splitting, smaller than observed for α-Fe, was in the range typical of the iron carbides [15]. The shape of the individual magnetic component indicated the presence of three distinct sextets. It is known that Mössbauer spectra of ε, χ, χ' and χ'' iron carbides contain three distinct sextets; while Mössbauer patterns of ε' and θ iron carbides appear as single sextet [16]. Reliable identification of different carbide phase is based on the number of constituent sextets, corresponding hyperfine magnetic fields, and their relative intensities. Compositional changes in terms of percent peak area of the different iron species as determined from curve fitting for all the samples along with corresponding sampling times are listed in Table 1 for the two temperatures used for the Mössbauer measurements.

During carbidization with CO, the catalyst was first transformed from hematite (Fe_2O_3) to magnetite (Fe_3O_4) and then reduced to iron carbide. The conversion of hematite to magnetite of this high surface area sample is generally rapid and difficult to monitor unless special attention is paid [17]. At the end of 24 h activation period (sample S-1, Table 1), the room temperature Mössbauer results revealed that about 85% of the iron in the catalyst was present as Hägg carbide (χ-Fe_5C_2), with the remaining iron present in a superparamagnetic (spm) form. Low-temperature (20 K) Mössbauer measurement of the same sample (i.e., sample S1) indicated that the spm phase was Fe_3O_4, and not the iron carbide, which can also be present in a spm phase. Combining the above results it is found that at the end of the 24 h activation with CO at 270 °C, the initial hematite converted to a mixture of 85% χ-Fe_5C_2 and 15% Fe_3O_4 which is in agreement to the results reported earlier [18]. A synthesis gas conversion of 85% was observed with this catalyst. Oxidation of iron carbide initially present after activation continues with the synthesis times and the amount of carbide phase gradually decreases with a corresponding increase of the fraction of Fe_3O_4 phase. Since the catalyst used in the present study was pure iron oxide without any promoter; the rate of re-oxidation of the carbides was rapid with 50% of iron in the sample S2 (collected after 28.9 h of FTS) found to be present as carbides while the rest was in an oxide phase. At the end of 311 h of synthesis time, the fraction of iron present as Fe_3O_4 was found to be 96% (sample # S5) with remaining iron in the spm phase; the synthesis gas conversion dropped to a level of about 16%. Low temperature Mössbauer results indicated that after 382.8 h of FTS, the phase composition of the catalyst (sample # S6) was 99% Fe_3O_4 and 1% spm phase which could be a surface carbide species.

Activation of iron-based catalysts for FTS is generally practiced with CO or syngas [10]. The iron oxide produced via in situ re-oxidation of carbide phase remains in contact with the syngas during FTS and fraction of the oxides can potentially be transformed to carbides (i.e., in situ regeneration). Since the present catalyst did not contain any structural promoter, the rate of in situ regeneration can be very small. Mössbauer spectra of sample S7 (collected after 481.6 h of synthesis) revealed that a small fraction of iron (about 5%) was present as hexagonal ε'-$Fe_{2.2}C$ phase. Activation of iron based catalyst with syngas is known to predominantly result in ε'-$Fe_{2.2}C$ [10, 19]. Hence, it is believed that the ε'-$Fe_{2.2}C$ phase observed in the present study was generated in situ by carbidization with syngas. No trace of χ-Fe_5C_2 phase was identified in any of the catalyst samples among S5–S8 by Mössbauer analysis and the major fraction of iron (about 90–95%) was found to be present as Fe_3O_4 (Table 1). The magnitude of CO conversion remained almost constant at around 10% during the 200 h of FTS period when these latter samples were collected. Thus, the presence of some fraction of iron carbide is necessary for a catalyst to exhibit high conversion. We consistently find that the aged sample of unpromoted catalyst has about 10–15% of the initial activity of the freshly carbided sample. Whether this activity is due to a residual surface layer of carbide or of Fe_3O_4 has not been defined.

3.3 Morphology and Phase Transformation by HRTEM, STEM and EELS

The morphology and phase transformation of the nano-catalyst during CO activation and FTS were studied by

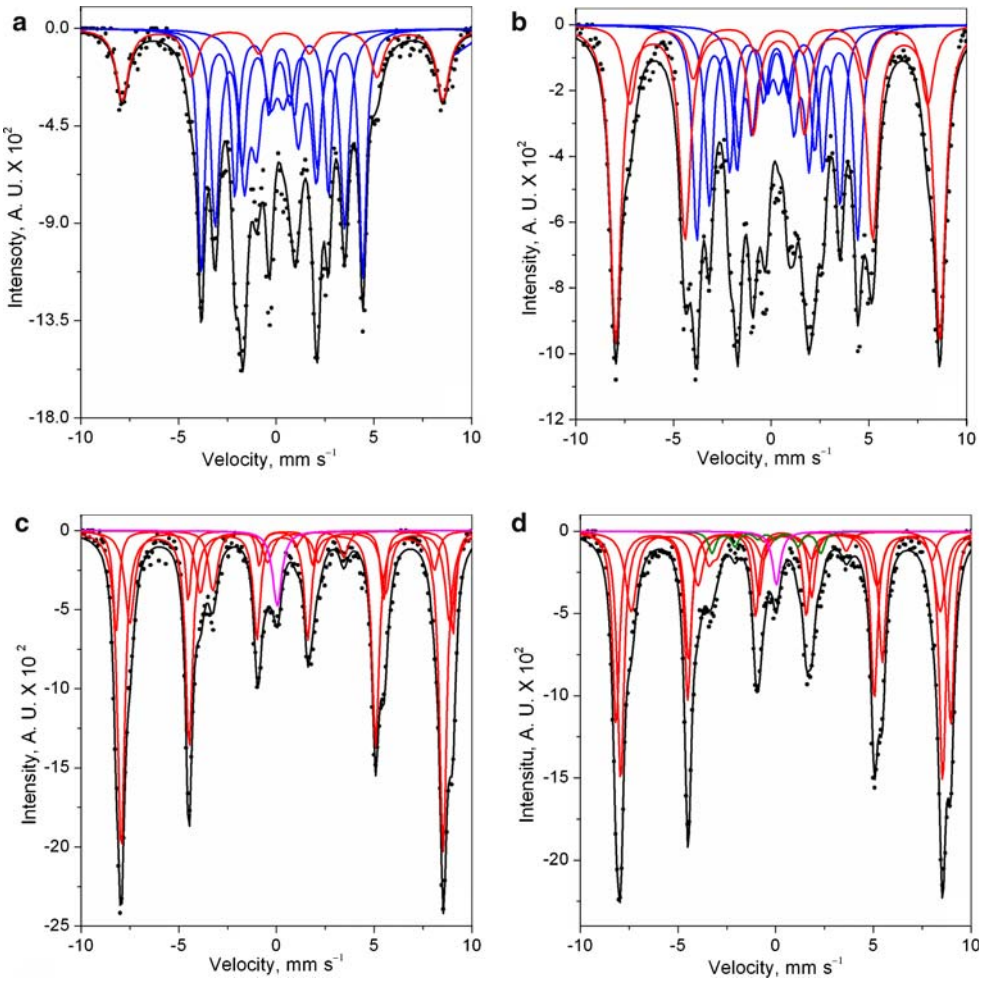

Fig. 2 Representative Mössbauer spectra of samples collected after activation and during FTS at 270 °C, 175 psig, $H_2/CO = 0.7$, and a syngas space velocity of 3.0 sl/h/g Fe: (**a**) sample S1 collected after carbidization with CO for 24 h at 270 °C, 175 psig, and a space velocity of 3.0 sl/h/g Fe; (**b**) sample S2 collected after 28.9 h of synthesis; (**c**) sample S5 collected after 311 h of FTS; and (**d**) sample S8 collected after 596.8 h of synthesis. The fitted curves are shown in solid lines: black, total spectra; red, oxide; blue, χ–Fe_5C_2; green, ε'-$Fe_{2.2}C$; and magenta, spm phase

Table 2 Summary of particle size distribution measurement result

FT synthesis time (h)	Mode (nm)	Median (nm)	$d_{1,0}$, nm ($\Delta d_{1,0}$, %)	$d_{3,2}$, nm ($\Delta d_{3,2}$, %)	$d_{4,3}$, nm ($\Delta d_{4,3}$, %)
0	19.02	18.05	19.15 (-)	23.48 (–)	25.86 (–)
112.6	25.5	25.75	27.24 (42.3)	34.04 (44.9)	41.04 (58.7)
258.3	26.05	28.17	30.48 (11.9)	41.73 (22.6)	49.02 (19.5)
406.3	41.51	35.54	36.14 (18.6)	51.88 (24.3)	58.79 (19.9)
505.6	36.51	40.41	44.29 (22.6)	65.35 (25.9)	75.68 (28.8)
620.8	46.5	51.97	57.15 (29.1)	82.52 (26.3)	99.89 (31.9)

The % increase of statistical diameters are calculated as: $\Delta d_{x,y} = \left[\left(d_{x,y}(t + \Delta t) - d_{x,y}(t)\right)/d_{x,y}(t)\right] \times 100$ where x = 1, 3, 4, and y = 0, 2, 3, respectively

HRTEM, STEM and EELS analysis. High-resolution STEM imaging coupled with EELS analysis was utilized to determine the chemical nature of any particular structure of interest in different catalyst samples mentioned in Table 1. To identify the elemental composition in EELS spectra, characteristic edge structure of Fe ($L_{2,3}$ edge at about 720–740 eV), oxygen (K edge at about 530–535 eV) and carbon (K edge at about 285–310 eV) are considered [20].

3.3.1 Morphology

The initial nano-particle catalyst had a narrow size distribution (3–5 nm) with a regular near-spherical morphology, as shown in Fig. 3. The vendor identified the as-received sample as γ-Fe_2O_3 based on electron diffraction pattern. γ-Fe_2O_3 has a simple cubic structure; hence, reflections from all the planes are possible. An electron microdiffraction pattern of the as-received material is shown

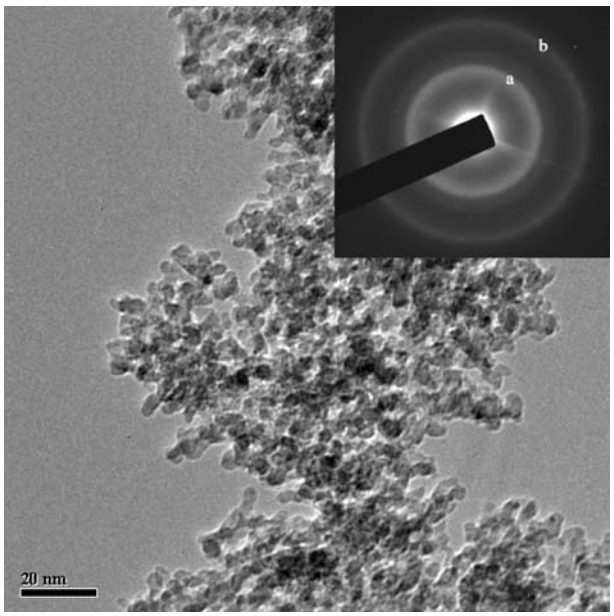

Fig. 3 TEM image of as received ultrafine iron NANOCAT® material. An electron microdiffraction pattern is also shown in inset. Diffraction rings are indexed as: a, and b from (311) and (440) faces of Fe_3O_4, respectively

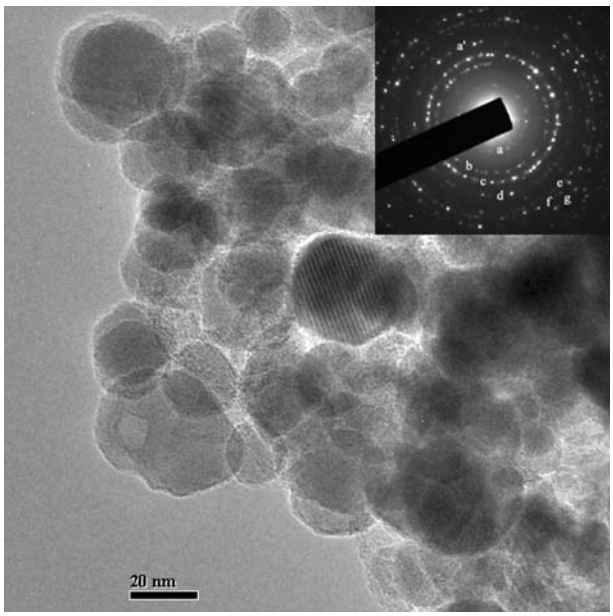

Fig. 4 TEM image of the nanocatalyst after CO activation for 24 h at 270 °C, 175 psig, and a space velocity of 3.0 sl/h/g Fe. An electron microdiffraction pattern is also shown in inset. Diffraction rings are indexed as: a′ from (510) face of χ–Fe_5C_2; a, b, c, d, e, f, and g from (111), (220), (311), (400), (422), (511) and (440) faces of Fe_3O_4, respectively

in Fig. 3 (inset) which exhibits diffuse rings. The distance from the center to the rings or diffraction spots is indicative of the lattice spacing of the particular crystallographic plane. Diffraction rings can appear for polycrystalline materials but those would be sharp and distinct with the continuous array of reciprocal-lattice points which are concentric spheres in reciprocal space indicating random orientation [21]. However, for amorphous materials where a lack of well-ordered crystal structure is evident, or materials containing nano-sized particles, these rings will be diffused. The diffuseness and variations in intensity profiles result from inelastic scattering phenomena.

The TEM image of the catalyst sample collected after CO activation for 24 h (sample S1) is shown in Fig. 4. The initial size of the nano-catalyst was in the range of 3–5 nm. Figure 4 reveals an increase in the particle size during carbidization. Formation of a crystalline structure is evident from this figure. Some of the particles were found to have an outer rim of 3–5 nm thickness. An electron microdiffraction pattern of the sample is also shown in Fig. 4 (inset). The diffraction pattern confirmed the presence of loose aggregates of iron carbides [22]. The magnetite particles yield well-defined spots in the diffraction pattern while the presence of carbide phase causes only diffuse rings originating from the presence of small particles. A high-resolution TEM image of this sample shown in Fig. 5 indicates well-defined crystalline structure with an outer rim of amorphous material having thickness of 3–5 nm. The chemical nature of this amorphous rim is critical for

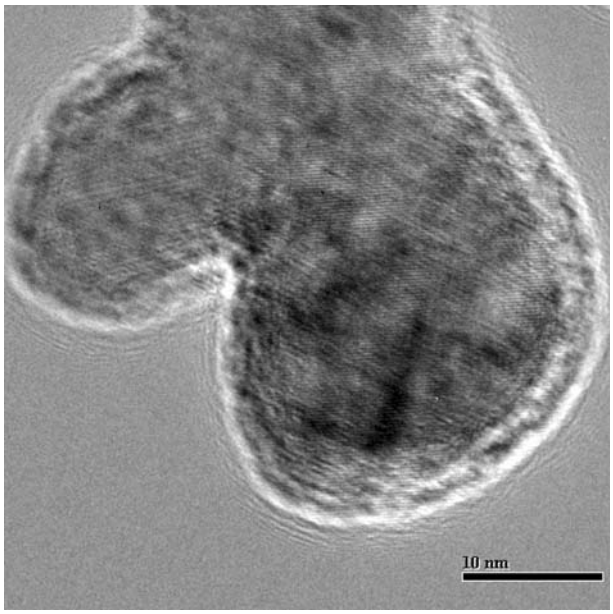

Fig. 5 High-resolution TEM image of the nanocatalyst after CO activation for 24 h at 270 °C, 175 psig, and a space velocity of 3.0 sl/h/g Fe. Well defined crystalline structure and an outer rim of amorphous material is evident

purpose of both catalyst characterization and activity considerations. High-resolution STEM and EELS measurements were used to identify the chemical composition of this rim. The amorphous outer rim is clearly evident

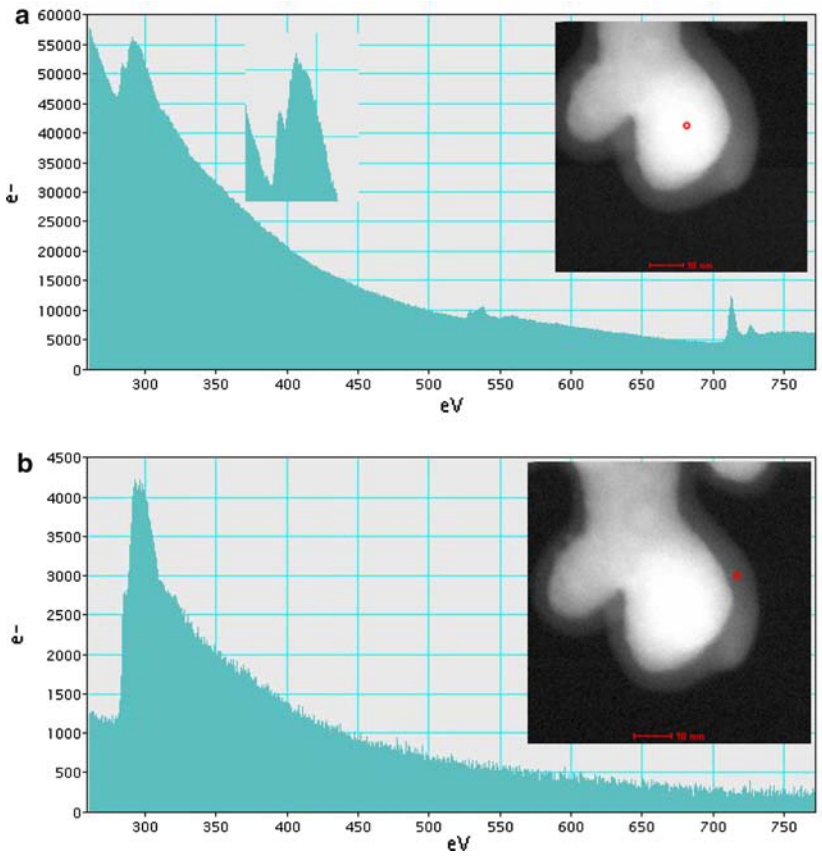

Fig. 6 EELS spectrum of the catalyst sample collected after CO activation for 24 h at 270 °C, 175 psig, and a space velocity of 3.0 sl/h/g Fe. High-resolution STEM images are shown in insets. The red dots in HRSTEM images indicate the position where the EELS spectra were recorded. A magnified view of carbon K-edge structure in the EELS spectra is also shown in (**a**) (inset)

from the high-resolution STEM images shown in Fig. 6a (inset) and b (inset). The red dots in these figures indicate the position where the EELS spectra were recorded (i.e., the electron beam was focused). The EELS spectra taken at the center of the particle indicates the characteristics edge structure of Fe $L_{2,3}$, oxygen K, and carbon K edge as presented in Fig. 6a. A magnified view of carbon K-edge structure in EELS spectra is also shown in Fig. 6a inset. Higher intensity of Fe and C edge spectrum over oxygen edge suggest that the particle is mainly composed of carbides and little oxide. The EELS spectra recorded at the center of outer rim as shown in Fig. 6b consists of only carbon K edge structure. Probing by EELS is a very sensitive technique and very low concentration of elements can be detected. The carbon K-edge structure clearly shows a weak π^* shoulder peak and an intense σ^* peak, which are characteristic of amorphous carbon species [20]. Since the EELS spectra of the rim do not contain any characteristic edge for Fe or oxygen, it can be concluded that the outer rim consists of amorphous carbon only.

A HRTEM image of another particle of sample S1 is presented in Fig. 7a which shows the particle are nano-

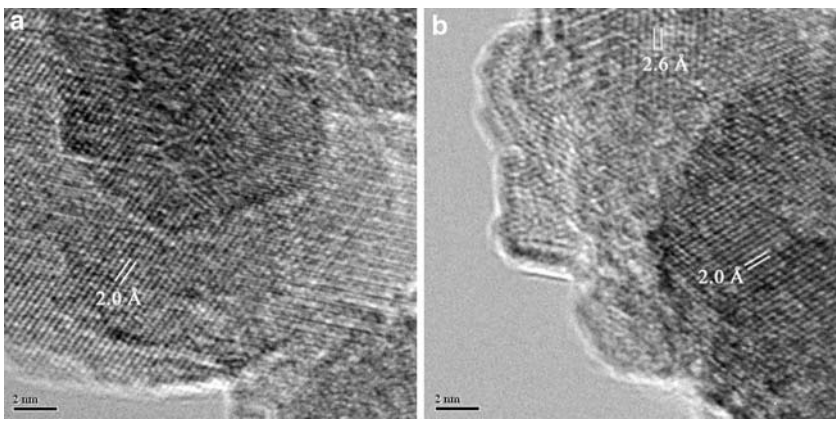

Fig. 7 HRTEM image of a particle of sample S1 (collected after carbidization with CO for 24 h at 270 °C, 175 psig, and a space velocity of 3.0 sl/h/g Fe): (**a**) nano-aggregates of iron carbides—the characteristic d-spacing of 2.0 Å can correspond to high intensity (510) or (021) plane of χ-Fe_5C_2; (**b**) nano-aggregates of iron carbides and oxide: the d-spacing of 2.6 Å can be assigned to high intensity (311) plane of Fe_3O_4

aggregates with atomic planes indicating crystalline structure. These structures originate from nanocrystalline grains within and on the nanoparticle surface. The carbide particles are made of aggregates of nanocrystals. Carbide particles formed in layers overlapping with each other as found by HRTEM (Fig. 7a). The characteristic d-spacing of these crystallites is 2.0 Å (which can correspond to high intensity (510) or (021) plane ofχ-Fe_5C_2 [23]). The non-smooth particles have a crumpled and boulder-like appearance and formed with different overlapping layers of iron carbides. However, HRTEM image of another portion of the same particle, shown in Fig. 7b, reveals two different types of crystal d-spacing—2.0 Å and 2.6 Å. The crystallite with characteristic d-spacing of 2.0 Å may represent iron carbide [24] as above while the one with a d-spacing of 2.6 Å can be assigned to high intensity (311) plane of magnetite. Coexistence of magnetite and iron carbides in the same particle indicate that oxide to carbide transformation during carbidization was not complete and the activated catalyst contains some amount of oxide which is in agreement with results obtained from Mössbauer analysis as shown earlier.

TEM image of sample S4 (collected after 167.7 h of synthesis) as shown in Fig. 8a indicates larger particles with irregular hexagonal shaped structures. Appearances of several small "nodule/bud" which are sprouted on the top of the larger particles are also evident. HRTEM image of a larger catalyst particle of this sample is presented in Fig. 8b which reveals a well defined single crystal of iron oxide (with a characteristic d-spacing of 2.6 Å corresponding to high intensity (311) plane of Fe_3O_4). No amorphous carbon rim outside this particle is observed. The initial wrinkled and boulder-like loose aggregates of multicrystalline iron carbides and oxides (as shown in Fig. 7a and b) transformed into a large single crystal of iron oxide.

A representative TEM image of sample S5 (collected after 311 h of FTS) is shown in Fig. 9a. Some of the particles from this figure have dimensions that are larger than 100 nm. The FTS was started with a catalyst having a size range of 3–5 nm. Thus, the appearance of such large particles clearly reveals that these are formed in situ during FTS. A high-resolution image of a particle from sample S5 is also shown in Fig. 9b. This image clearly shows a single crystal iron oxide (with a characteristic d-spacing of 2.6 Å corresponding be high intensity (311) plane of Fe_3O_4) core by an external well-ordered graphitic carbon layer of thickness about 5 nm.

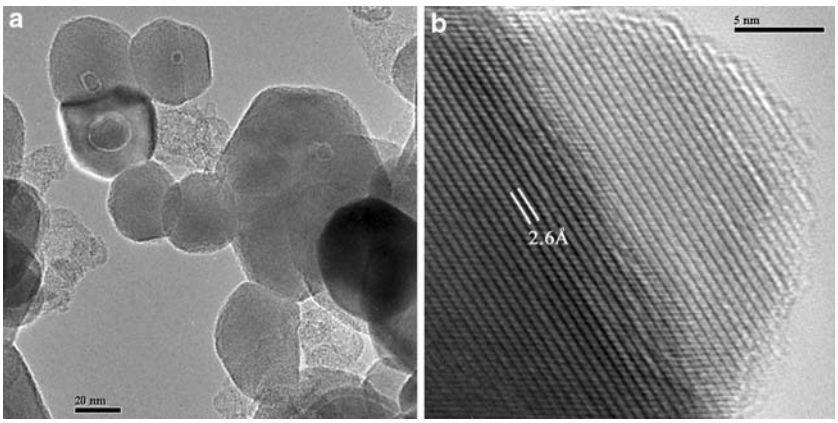

Fig. 8 TEM image of a particle of sample S4 (collected after 167.7 h of FTS at 270 °C, 175 psig, and a syngas space velocity of 3.0 sl/h/g Fe): (**a**) appearance of several small "bud" sprouted on the top of the bigger particles with irregular hexagonal shape structure; (**b**) well defined single crystal of iron oxide (with a characteristic d-spacing of 2.6 Å corresponding be high intensity (311) plane of Fe_3O_4)

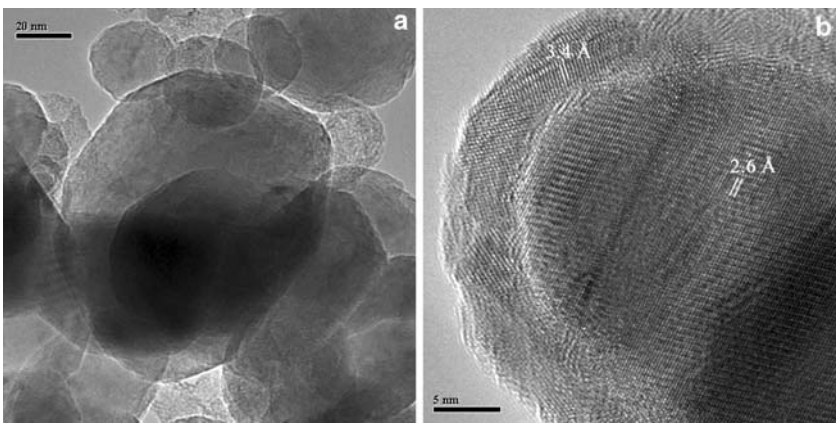

Fig. 9 HRTEM image of a particle of sample S5 (collected after 311 h of FTS at 270 °C, 175 psig, and a syngas space velocity of 3.0 sl/h/g Fe): (**a**) big particles with largest dimension higher than 100 nm; (**b**) single crystal of iron oxide (with a characteristic d-spacing of 2.6 Å corresponding to high intensity (311) plane of Fe_3O_4) is encapsulated with well ordered graphitic carbon rim of thickness about 5 nm

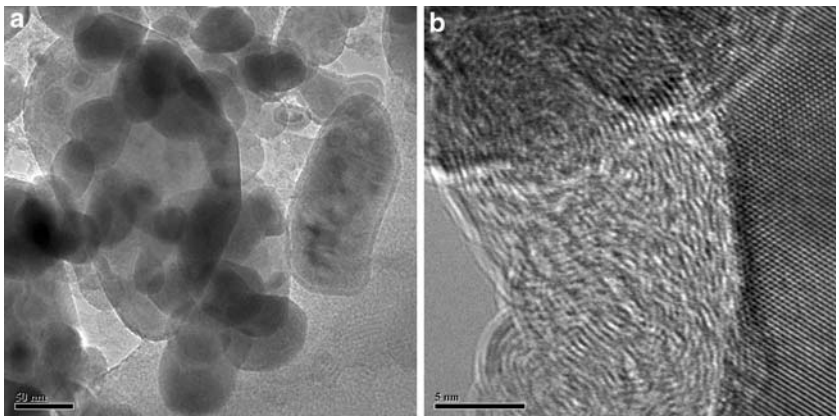

Fig. 10 HRTEM image of a particle of sample S6 (collected after 596 h of FTS at 270 °C, 175 psig, and a syngas space velocity of 3.0 sl/h/g Fe): (**a**) large single crystal with largest dimension larger than 150 nm and some of the particle have outer rim structure; (**b**) single crystal of iron oxide covered with an outer layer of amorphous carbon of thickness about 10 nm

The TEM images of sample S6 (collected after 596.8 h of FTS) is shown in Fig. 10a. The presence of a large single crystal with a dimension greater than 150 nm can be noticed. The presence of an outer carbon rim structure on some of the particles is also evident. High-resolution TEM image of a particle from sample S6, as presented in Fig. 10b, clearly shows that a single crystal of iron oxide is covered by a layer of ordered graphitic carbon of thickness about 10 nm. The thickness of the carbon rim around the particle does not grow above about 10 nm. Hence, the appearance of the larger particles does not originate from the deposition of carbon on the catalyst particles; non-etheless, it is indicative of nano-scale growth of individual catalyst particle.

3.3.2 Phase Transformation

An effort has been made to study the in situ reoxidation mechanism of iron carbides during FTS. A high-resolution TEM image of a particle from sample S2 (collected after 28.9 h of FTS) is presented in Fig. 11. The image shows that the particle has an outer rim of thickness about 5 nm. The spreading of the material forming the rim around the particle and the adjacent particle suggest that it is not the amorphous carbon rim as described above. This rim may originate from leftover wax produced during FTS and remained during *o*-xylene extraction step. In this case this rim will act as a protective layer and prevent aerial oxidation during catalyst characterization. The distribution of the crystalline zone in this particle reveals two concentric nano-regions with two distinct crystal axis spacing—the inner crystalline core has a characteristic d-spacing of 2.6 Å (can correspond to high intensity (311) plane of Fe_3O_4) and the outer crystalline region consists of a characteristic d-spacing of 2.0 which can be assigned to high intensity (510) or (021) planes of χ-Fe_5C_2 [23]. The zone boundary of these two nano-regions (as indicated by a white circle in Fig. 11) reveals a sharp change in the magnitude of characteristic d-spacing values indicated above. The iron oxide encapsulated by iron carbide

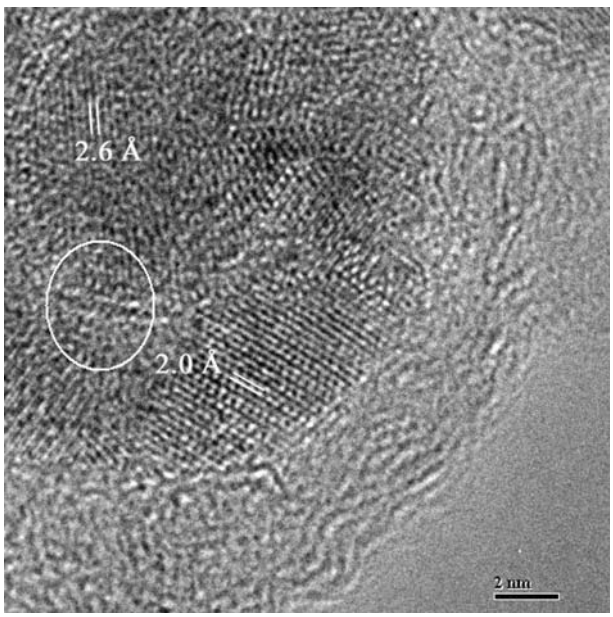

Fig. 11 HRTEM image of a particle of sample S2 (collected after 28.9 h of FTS at 270 °C, 175 psig, and a syngas space velocity of 3.0 sl/h/g Fe): concentric crystalline nano-regions of iron oxide and carbide. The inner oxide core is encapsulated by an outer carbide core

concentric layers significantly indicates a definite pattern in the in situ reoxidation phenomena during FTS and will be described in the Discussion section.

Appearance of small "buds" on large particles in the TEM image of some samples has been observed. HRS TEM-EELS measurement was used to identify the chemical nature of these large particles and the small buds. Figure 12a represents the EELS spectra of a large particle carrying a "small bud" on the surface (sample after 311 h of FTS). A high resolution STEM image of this particle is also shown in Fig. 12a (inset) where the red dot indicates the point of focus for recording EELS spectrum. Presence of characteristics EELS edge structure of Fe $L_{2,3}$ and oxygen K edge and the absence of carbon K edge structure shows that the particle is an iron oxide. The characteristic

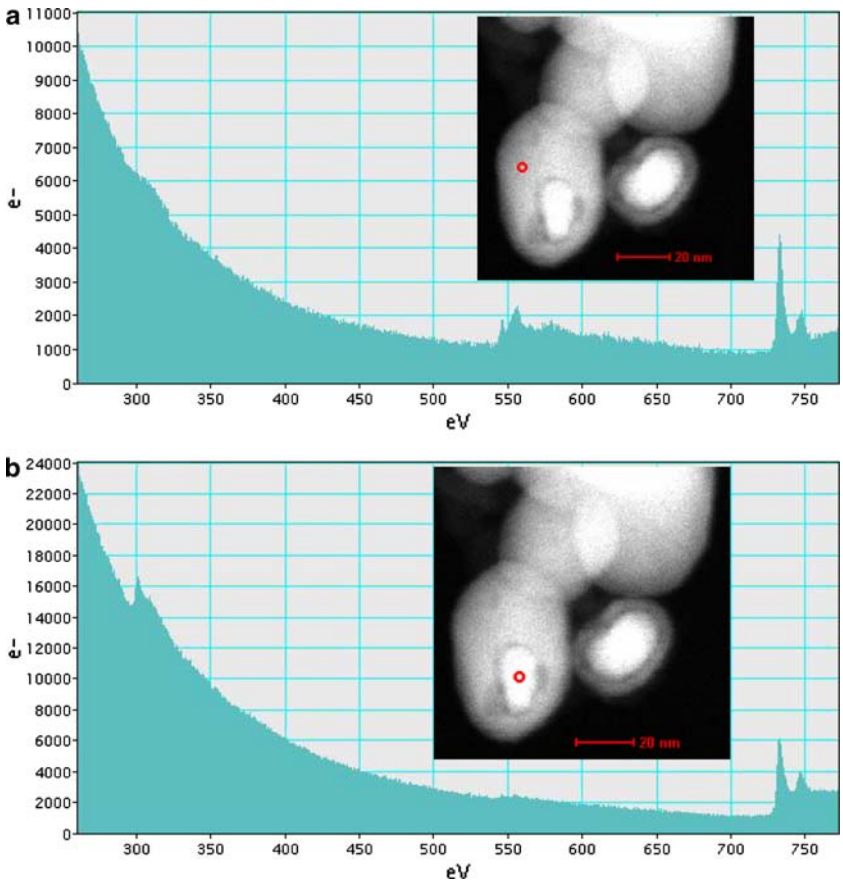

Fig. 12 STEM-EELS measurements of the catalyst sample collected after FTS for 311 h at 270 °C, 175 psig, and a syngas space velocity of 3.0 sl/h/g Fe. High-resolution STEM images are shown in insets. The red dots in HRSTEM images indicate the position where the EELS spectra were recorded

shape of Fe $L_{2,3}$ edge in the EELS spectrum reveals the presence of magnetite [25]. However, similar HRSTEM-EELS analysis of the nodule sprouted on the large particle as shown in Fig. 12b indicates the presence of only Fe and carbon edge structure in the EELS spectrum. The point of electron beam focus is shown in Fig. 12b (inset) by a red dot. This data clearly reveal that the small buds are composed of iron carbides. It was reported that while using particles of 100–300 μm in size, the carbide phase forms as small nodules on the surface of the magnetite and the phase transformation proceeds slowly into the bulk [4, 7]. However, such phenomena were not observed in the present study. It was not possible to determine the physical nature of attachment of these small carbide buds to the large magnetite particles in the present study. The presence of very few small buds on the surface of the large particles suggests that the small carbide nodules are only physically supported on the large magnetite particle without chemical or other type of binding between them.

3.4 Particle Size Distribution: Nano-scale Growth

The size of a spherical (equi-dimensional) homogeneous particle can uniquely be specified by its diameter while for any regular compact particle (e.g., cube, tetrahedron) a single dimension cannot be used to define size. A single irregular particle has an infinite number of linear dimensions and it is only when selected dimensions are averaged that a meaningful value results. To specify "true representative size" of any irregular shaped particle, some approximations are required. Particles that are non-equidimensional are often characterized by specifying the second largest dimension also. Particle sizing by microscopy involves in observation and measurement of individual particles with each measurement quantifying the particle size in only one direction. If the particles are in random orientation, and if sufficient particles are counted, then the results of these measurements reflects the size distribution of the projected areas of the particles (assuming stable orientation) perpendicular to the viewing direction (i.e., plane of photo). Since, the particle sizes in the present study are measured from the HRTEM images, a statistical diameter, the Feret diameter, defined as the distance between pairs of parallel tangents to the projected outline of the particles on the plane of photo [26], is used to specify the particle size. Since the particles were non-equidimensional, the arithmetic average of the largest Feret diameter in *x*- and *y*-axis was considered as the "representative particle diameter" of an individual particle. For each catalyst sample mentioned in Table 1, a large number

of particles (about 1,200–1,500 particles per sample) were counted and their individual Feret diameter was determined. Having defined the relevant particle size, the relative frequency $(n_i/\sum n_i)$ of this occurrence in each representative size range was calculated and continuous, normalized relative frequency distributions (particle size distribution, PSD) were generated for each sample assuming the following relations:

$$\sum_{i=1}^{n} f(x_i) = 1; \text{ and } F(x) = \sum_{j \le x} f(j)$$

Once the PSD is determined, several average statistical parameters are considered to quantify any change in average particle size of catalyst particles during FTS. Since the PSD in the present study is of interest to the active surface area of the catalyst particles, these parameters include (a) mode (the most commonly occurring particle size) of the distribution; (b) median (the 50% size on the cumulative PSD curve) of the distribution; (c) number mean diameter ($\bar{x}$ or $d_{1,0}$), the center of gravity of the number distribution; (d) surface area moment mean diameter ($d_{3,2}$) or Sauter mean diameter (SMD)—the average diameter based on unit surface area of a particle; and (e) volume moment mean diameter ($d_{4,3}$)—the average diameter based on the unit volume of a particle. For the number mean diameter ($\bar{x}$) of the distribution, the moment of the sums of the elementary areas of the relative frequency distribution of width ∂x, about the ordinate, equals the sum of the moments of the elements about the ordinate [26]:

$$\sum_{0}^{\bar{x}} (x - \bar{x}) \frac{d\phi}{dx} \partial x = \sum_{0}^{\bar{x}} (\bar{x} - x) \frac{d\phi}{dx} \partial x \Rightarrow$$

$$\bar{x} \sum_{0}^{\bar{x}} d\phi = \sum_{0}^{\bar{x}} x d\phi \Rightarrow \bar{x} = \frac{\sum x d\phi}{\sum d\phi} = \frac{\sum x dN}{\sum dN}$$

where ϕ is the cumulative number frequency, x is the particle size in nm and for a number distribution $d\phi = dN$. The SMD and volume moment mean diameter were calculated according to the following equations [26]:

$$d_{3,2} = \frac{\sum d_i^3 N_i}{\sum d_i^2 N_i}; d_{4,3} = \frac{\sum d_i^4 N_i}{\sum d_i^3 N_i}$$

where d_i is the particle diameter, and N_i is the number of particles of size d_i.

The PSD in terms of relative number frequency of different catalyst samples are shown in Fig. 13a–f and the results of PSD analysis are presented in Table 2. The PSD of all the six samples in terms of cumulative number frequency are presented in Fig. 14. The results reveal a significant increase in the representative diameters ($d_{1,0}$, $d_{3,2}$, and $d_{4,3}$) and other statistical parameters of the PSD for catalyst sample with synthesis time. The percent increase in the three statistical diameters are also presented in Table 2 which clearly indicates continuous nano-scale growth of particles during FTS. Cumulative number frequency distribution shown in Fig. 14 reveals that for a certain cumulative fraction, the corresponding representative size of the catalyst particles increase with synthesis time. Appearance of larger particles in the HRTEM images also suggests nano-scale growth of particles during FTS. The frequency distribution plots shown in Fig. 13a–c indicate unimodal distribution of particle size with the width of distribution increasing with the synthesis time. The PDS plots for these samples reveal predominantly growth of particles. However, the PSD plot presented in Fig. 13d and e clearly indicate a bimodal distribution of particle size. This bimodal distribution likely arises from growth of smaller particles and simultaneous nano-scale attrition or breakage of bigger particles already present in the system. This growth and breakage phenomena occur simultaneously and the frequency distribution reaches a quasi-equilibrium stage. At this point the distribution becomes unimodal and the width of the PSD should reach a maximum, as shown in Fig. 13f.

4 Discussion

Phase transformation during activation and evolution of active phase under FTS determine the performance of the catalyst. It is known that during the activation (using either CO, H_2 or syngas) process, iron oxide (hematite, α-Fe_2O_3) transforms quickly to magnetite (Fe_3O_4), which converts to different iron phases depending on activation environment. Activation using H_2 results in metallic iron (Fe^0), which evolves slowly into mixture of iron carbides and oxides on exposure to syngas during FTS [27]. When CO or syngas is used for activation, based on initial composition of the catalyst, different types of iron carbides have been identified [5, 10, 28].

Rao et al. [18] has reported that 24 h CO activation of a promoted iron catalyst (Fe/Cu/K/Kaolin) results in only χ-Fe_5C_2. When the same catalyst was activated with syngas, both χ-Fe_5C_2 and ε'-$Fe_{2.2}C$ was identified. No ε'-$Fe_{2.2}C$ was detected in samples collected during carbidization using CO [19]. However, activation of iron based catalyst with syngas predominantly results in ε'-$Fe_{2.2}C$ [10, 19]. In general, CO activation was found to lead to a higher fraction of carbide phase and to a somewhat higher catalytic activity than similar syngas or H_2 activation. The fraction of iron present as the carbide following the activation was found to be dependent on catalyst composition. Rao et al. [19] studied the activation of a promoted

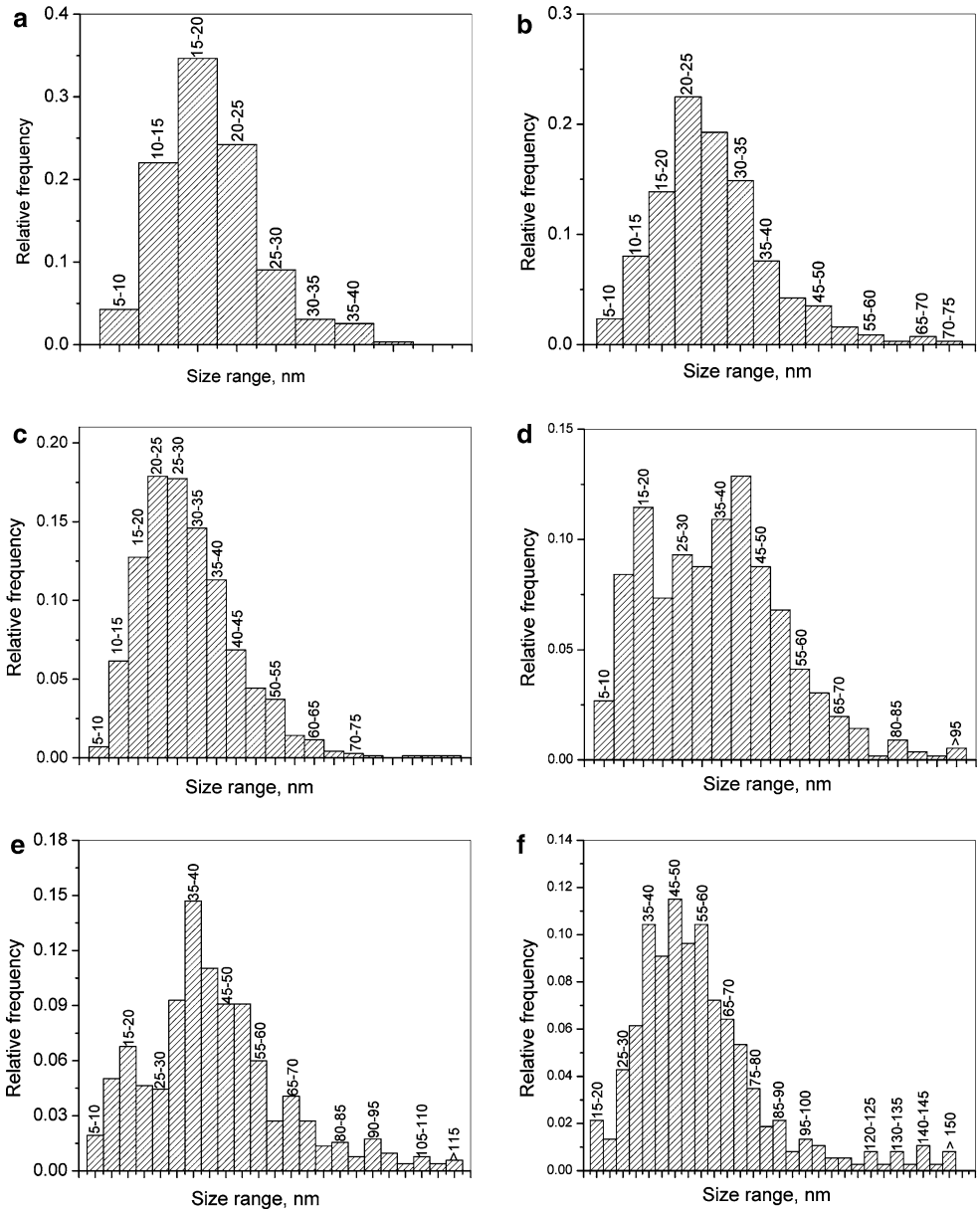

Fig. 13 Relative particle size distribution of catalyst samples collected at different time-on-stream during FTS at 270 °C, 175 psig, and a syngas space velocity of 3.0 sl/h/g Fe: (**a**) after CO activation for 24 h; (**b**) 112.6 h; (**c**) 258.3 h; (**d**) 406.3 h; (**e**) 505.6 h; (**f**) 620.8 h

iron-based catalyst using syngas at 280 °C and 150 psig. Mössbauer characterization of the catalyst sample collected after 12.5 h of carbidization indicated a phase composition of 23% ε′-$Fe_{2.2}C$, 12% χ-Fe_5C_2 and 17% spm phase. Zarochak and McDonald [29] studied the effect of pretreatment on the activity and the selectivity of slurry phase FTS with a potassium promoted precipitated iron catalyst and characterized the catalyst by Mössbauer spectroscopy. Prior to FTS the catalyst was activated for 24 h using CO and syngas. It was found that the catalyst activated in CO was completely converted to χ-Fe_5C_2 while the catalyst activated in syngas was converted partly to ε′-$Fe_{2.2}C$ during 24 h activation, and was completely converted to ε′-$Fe_{2.2}C$ only after 503 h of FTS. The FTS activity and stability of the catalyst subjected to CO pretreatment was found to be higher than that found for the catalyst activated in syngas.

Analysis of simultaneous reaction kinetics, Mössbauer and X-ray diffraction measurements have indicated a linear relation between the amount of bulk carbide content of the catalyst and FTS rate [15, 30]. Phase composition of unpromoted precipitated Fe catalysts were studied during various periods of FTS by Li et al. [31] using Mössbauer spectroscopy, XANES and EXAFS techniques. Activation in CO was found to transform the initial oxide into χ-Fe_5C_2 while Fe_3O_4 was the only detectable iron phase after 450 h of FTS. Bulk Mössbauer and X-ray absorption spectroscopy results revealed a consistent decrease in carbide

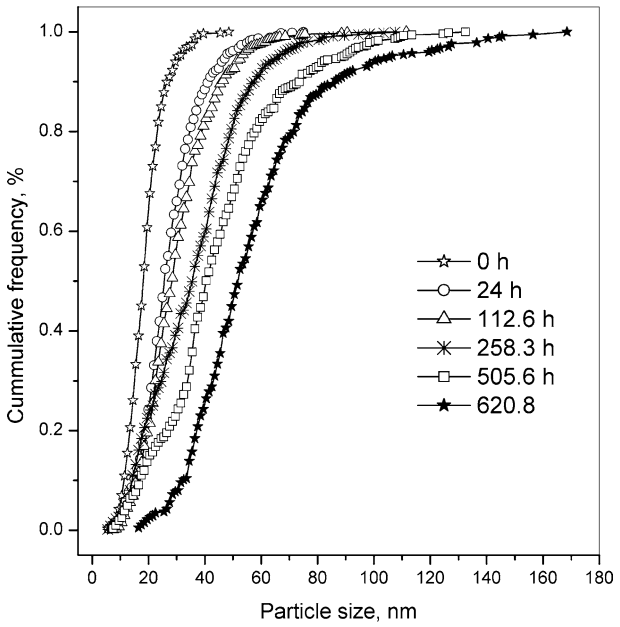

Fig. 14 Cumulative number frequency distribution of the catalyst sample collected at different time-on-stream during FTS at 270 °C, 175 psig, and a syngas space velocity of 3.0 sl/h/g Fe

concentration with FTS time while the CO conversion decreased by a factor of 10 during the structural evolution of almost purely iron carbide (after CO activation) to pure Fe_3O_4 (after 450 h of FTS). Based on the above results it was concluded that re-oxidation of carbides and catalyst deactivation are concurrent processes caused by changes of chemical potential of absorbed species at the carbide surface, which render higher concentration of oxidizing species on surface than in the adjacent gas phase [31]. These conditions, in turn, lead to the oxidation of carbides even in the reducing environments (i.e., presence of syngas). H_2O and CO_2 produced in FTS is generally considered as an oxidizing agent for the iron carbides [27].

The results obtained from Mössbauer analysis are consistent with the above mentioned results. χ-Fe_5C_2 was the only carbide phase detected in the present study after carbidization of unpromoted iron catalyst using CO for 24 h. The carbides can be oxidized during FTS via two processes: (a) the reaction of in situ generated water vapor with carbides to produce in one case magnetite and elemental carbon and in the other magnetite and methane; and (b) the reaction of hydrogen with carbidic or elemental carbon to form methane. Re-carbidization of produced magnetite at the surface in contact with syngas (i.e., under reducing environment) can regenerate some carbide phase during FTS. This situation will be somewhat similar to activation of catalyst using syngas except that a parallel oxidation reaction will compete with the re-carbidization. Small fraction of (about 5%) hexagonal ε'-$Fe_{2.2}C$ phase was identified in some samples collected after 480 h of FTS. This carbide phase is believed to be generated via in situ re-carbidization of magnetite by syngas. The magnitude of regeneration of the carbide phase depends on the amount and type of promoters present in the catalyst. Since the catalyst used in the present study did not contain any promoter, the rate of re-carbidization is expected to be slow. The rate of disappearance of carbide phase with FTS was also found to be rapid in the present study. The catalytic activity at this point was found to be lower by a factor of almost 10 as compared to fresh (CO activated) catalyst.

Mössbauer analysis is informative about the changes in bulk phase composition of iron catalysts which may not directly track the catalytic activity. The presence of small amounts of surface carbide which may not be detected by Mössbauer spectroscopic measurement can result in lower conversion levels. Li et al. [32] claimed that even carbidization of only a near-surface region in bulk Fe_3O_4 is sufficient to achieve steady-state FTS turnover rates. The above conclusion was drawn based on methane formation rate up to 15 h of synthesis time which may not necessarily represent a steady-state result. Moreover, methane is not a representative Fischer–Tropsch product because it is not formed from the polymerization of the monomeric $–CH_2–$ units. Nevertheless, it should be emphasized that true steady-state activity (and selectivity) of iron catalyst is not reached in minutes or hours but rather over periods of several hundred hours [33]. Results from the present study indicate that it is necessary for some carbide to be present to have a catalyst with a high activity; however, it was evident that the activity of the catalyst cannot be predicted solely from the fraction of iron that is present as the carbide.

Integral FTS rates decreased by almost a factor of 10 leading to a decrease in CO conversion from 85% to 9.8% after 597 h on-stream (Fig. 1). It is evident from the results that the change in chemical composition of catalyst (i.e., iron carbide to magnetite) has a major role for such a significant decrease in activity. The high conversions in the early stages of the reaction can lead to higher H_2O/H_2 and/or CO_2/CO ratios (depending on water-gas shift activity of the catalyst) than those present at low conversions at later reaction times. Hence the oxidizing potentials of the reactant–product mixtures in the gas phase and in the liquid phases in equilibrium with this gas phase may be significantly higher during the early stages of the experiment. This higher concentration may also be present at the center of a catalyst particle. Although CO_2 can lead to the oxidation of iron carbides, Li et al. [31] reported that during FTS using unpromoted, precipitated iron catalyst, the presence of added $CO_2(CO_2/CO = 0.3)$ in the feed gas did not influence CO conversion rates (or apparently alter the structure of the catalytic phases). Hence, CO_2 can be

regarded as essentially inert at reaction conditions used for the present study. Li et al. [31] have also discussed possible transformation pathways of re-oxidation of iron carbides during FTS. They eliminated the possibility of nucleation of re-oxidation at surface (surface oxidation) and claimed that re-oxidation and deactivation is caused by changes of chemical potential of absorbed species at the carbide surface which render higher concentration of oxidizing species on the surface than in the contacting gas phase, thus preventing re-carbidization in the FTS environment.

The surface and bulk composition of a catalyst during steady-state FTS is determined by a balance among several simultaneous processes which include the amount of CO that is converted to products in the Fischer–Tropsch and the water-gas shift reactions, and the amount of CO that is dissociated on the catalyst surface in a form that maintains the carbide phase. Any imbalance between these rates would lead to the net introduction or removal of carbon or oxygen atoms into the inorganic structure, and to the dynamic interconversion of iron oxides and iron carbides. It has been reported [32] that magnetite crystallite become almost immediately active after exposure to syngas and incipient conversion of near surface oxide layers to iron carbides can produce a low magnitude of methane production.

We were able to successfully identify some catalyst particle at initial synthesis period which has a tiny iron oxide core and an outer iron carbide layer (Fig. 11). However, after 250 h of synthesis time, only single crystal large magnetite particles were observed. Appearances of very small iron carbide particles were also noticed. The water produced via FTS in the outer rim of any particle can escape easily while the water produced at the center of the particle needs to diffuse out. Also the outer surface of the particle is in contact of syngas (i.e., under reducing environment), which can potentially replenish the carbide surface (re-carbidization). On the contrary the center of the particles may be in an oxidizing environment (high concentration of water and CO_2 and low concentration of CO and H_2). Considering the above facts, it is believed that the nucleation of re-oxidation starts at the center of the catalyst particle. Since this catalyst is unpromoted, the rate of re-carbidization is slower than the rate of re-oxidation. The magnetite core grows larger. Some surface carbide species can be generated, or regenerated, when these larger magnetite particles come into contact with syngas which in turn can result in a low conversion (ca. 10% as observed experimentally) for a long period of synthesis time. This dynamic surface inter-transformation between carbide and oxide phase may produce a low steady conversion, although the bulk composition of catalyst remains primarily magnetite.

Appearance of amorphous and graphitic carbonaceous compounds on the surface of supported/unsupported and/or promoted/unpromoted iron catalysts have been reported by several researchers [7, 15, 33–36]. Dwyer and Hardenbergh [36] reported the formation of graphite-like carbonaceous compound on an Fe foil used for FTS reaction by in situ XPS and observed that the deactivation of the Fe foil catalyst is accompanied with an increase of the C 1 s peak intensity for the graphite-like carbonaceous compound. However, Shroff et al. [7] reported the formation of an amorphous carbon layer on iron carbide particles during the FTS reaction with precipitated iron based catalyst while Jin et al. [37] from the same research group observed the appearance of large amounts of the graphitic carbon layer on a catalyst pretreated by CO at a higher temperature (773 K). Bartholomew and co-researchers [33, 35] indicate that they have identified and quantified up to six different carbonaceous species in the iron-based catalysts after FTS reaction. The reactivity of these species was assigned from the temperature value of the methane formation peak in the temperature-programmed surface reaction with hydrogen (TPSR-H_2); that is, the more reactive the species, the lower the methane formation temperature. They suggested a series of transformation of C_α (atomic carbonaceous species, and lightly polymerized surface carbon species formed by CO dissociation on the catalyst surface) to ε'-$Fe_{2.2}C$ and then to χ-$Fe_{2.5}C$. It was also proposed that the ε'-$Fe_{2.2}C$ to χ-$Fe_{2.5}C$ transformation might occur through precipitation of graphitic carbon. Niemantsverdriet et al. [15] claimed that the deactivation of a precipitated iron catalyst activated in H_2 is caused by the formation of inactive carbon (graphite like) that blocks the active sites of the iron carbides.

The appearance of both amorphous and well-ordered graphitic carbon layers on the surface of nano-catalysts in the presence of syngas has been observed. No graphitic carbon phase was identified after CO activation of the catalyst. When amorphous carbon rims were observed, the composition of the core was identified as iron carbide and the particle sizes were found to be relatively smaller. When graphitic carbon rims were identified, the particles were quite large and the core was identified as pure magnetite (Figs. 9b and 10b). The surface of magnetite particles was always found to be free from amorphous carbons.

Both graphitic and amorphous carbons affect the high-energy loss portion of the EELS spectrum at the carbon K-edge. The morphology of amorphous and crystalline carbon is determined by the fraction of sp^3-bonded carbon. The differences between the EELS spectra of graphitic and amorphous carbon are due to differences in carbon-carbon bonding. The relative intensity of carbon $1s \rightarrow \pi^*$ and $1s \rightarrow \sigma^*$ core-level transitions provides a robust measure of the percentage sp^2-bonded carbon. A strong π^* peak

suggests that the material is primarily sp^2-bonded. Due to more ordered crystal structure and regular bonding, the spectra of both ordered and disordered graphite show a sharp π^* peak followed by a higher energy wide, flat-topped σ^* peak [38]. At the front edge of the σ^* peak is another sharp peak called the "A" peak. The EELS spectrum for amorphous carbon, however, only has a small π^* shoulder, a sloping σ^* peak, and no "A" peak.

The relative intensity of π^* (at 284 eV) to σ^* (at 292 eV) peak and a strong π^* peak in the carbon K-edge EELS spectrum (Fig. 6a) recorded at the center of the catalyst particle indicates well-defined crystalline structure of iron carbide. When the electron beam was focused in the outer rim of the particle, the carbon K-edge fine structure (Fig. 6b) reveals an intense σ^* peak (at 295 eV) and a weak π^* shoulder peak (at 285 eV) only. This clearly indicates the presence of amorphous carbon in the outer carbon ring.

The appearance of well-ordered crystalline graphitic carbon phase on single crystal magnetite particles are evident from the HRTEM images shown in Figs. 9b and 10b. These graphitic carbon layers can inhibit the re-carbidization of magnetite in the FTS environment and results in permanent catalyst deactivation. The surface carbon layers (amorphous and graphitic) can be formed by disproportionation of CO as: $2CO \leftrightarrow CO_2 + C$ (Boudouard reaction) or inter-conversion of iron carbides [33]. At higher conversion level (as the initial period of the present study), according to surface carbide mechanism, the dissociated CO species can be rapidly converted into hydrocarbon products (–CH_2– units). However at lower conversion levels (typically 10–20%), the surface carbon species may not be converted to hydrocarbon products and may enrich the catalyst surface. This situation will be favorable for the graphitization of the surface carbonaceous compounds resulting in catalyst deactivation and further lowering of CO conversion. In other words, the FTS reaction at quite lower conversion levels could facilitate the formation of the graphitic carbon as observed in the low conversion period of the present study.

Combining the results from Mössbauer, EELS, HRTEM and PSD measurements it was found that all the larger particles grown during FTS are single crystal magnetite. On the contrary, the ultrafine particles were found to be iron carbides. No single larger particle of iron carbide was observed. This strongly suggests that either the nano-scale growth of particles continues with a simultaneous transformation of iron carbide to oxide or the two phenomena occur in successive steps. If the reverse phenomena would have been true, then at least a few of larger particles formed in situ should have been composed of iron carbide. The polycrystalline structure of iron oxides used in the current study is also favorable for diffusion along grain boundaries [39]. The iron carbide is believed to transform into iron oxide first and then its growth continues.

5 Conclusions

CO activation of unpromoted ultrafine iron nanocatalyst for 24 h converts the hematite into a mixture of 85% χ-Fe_5C_2 and the remainder to magnetite. FTS using this catalyst results in an initial high conversion (ca. 85%) of CO and H_2. However, the conversion decreased by a factor of almost 10 over 400 h of synthesis time and after that remained constant (ca. 10%) up to 600 h of FTS. Mössbauer and EELS measurements revealed that catalyst deactivation was accompanied by structural evolution of the catalyst from initial nearly pure iron carbides (after CO activation), to their gradual in situ re-oxidation, and ultimate transformation to nearly pure magnetite after 400 h of synthesis time. It is concluded that for an iron based catalyst to exhibit high activity in FTS, the carbide contents of the catalyst should be reasonably high. Experimental data suggest that the nucleation for carbide/oxide transformation initiates at the center of the particle. It is believed that the re-oxidation is caused by high concentrations of water produced during FTS. Small amounts of ε'-$Fe_{2.2}C$ were detected in some samples collected after 480 h of FTS. These carbide species are believed to be generated by syngas during FTS. PSD measurements indicate growth of individual catalyst particles. Statistical average diameters were found to increase by a factor of 4 over 600 h of synthesis time. The breadth, mode and median of PSD were found to increase continuously with time-on-stream. Some particles with a dimension larger than 150 nm were also observed. Chemical compositions of the larger particles were found to be pure single crystal magnetite by EELS measurements. A small number of ultrafine carbide particles was identified in the catalyst samples collected during the later period of FTS. It appears that carbide/oxide transformation and nano-scale growth of particles continued either in series or simultaneously; but definitely not in the reverse order since in that case some larger carbide particles would have been observed. EELS-STEM measurements reveal amorphous carbon rims of thickness of 3–5 nm around some particles after activation and during FTS. Well ordered graphitic carbon layers on larger single crystal magnetite particles were found by EELS-STEM measurement. The maximum thickness of the carbon (amorphous or graphitic) rim does not grow above about 5 nm. Thus the growths of particles are not due to carbon deposition.

Acknowledgement We acknowledge financial support for this work from U.S. Department of Energy (under contact DE-FC26-03NT41965) and the Commonwealth of Kentucky.

References

1. Wender I (1996) Fuel Proce Technol 48:189
2. Steynberg AP (2004) In: Steynberg AP, Dry ME (eds) Fischer–Tropsch technology, Stud Surf Sci Catal, vol 152. Elsevier, USA, p 8
3. Sarkar A, Neathery JK, Davis BH (2007) Separation of Fischer–Tropsch wax products from ultrafine iron catalyst particles, US DOE Final Technical Report, Contract # DE-FC26-03NT41965
4. Li S, Ding W, Meitzner GD, Iglesia E (2002) J Phys Chem B 106:85
5. Huang C-S, Ganguly B, Huffman GP, Huggins FE, Davis BH (1993) Fuel Sci Technol Int 11(9):1289
6. Zhao R, Goodwin JG, Jothimurugesan K, Gangwal SK, Spivey JJ (2001) Ind Eng Chem Res 40:1320
7. Shroff MD, Kalakkad DS, Coulter KE, Köhler SD, Harrington MS, Jackson NB, Sault AG, Datye AK (1995) J Catal 156:185
8. Pham HN, Datye AK (2000) Catal Today 58:233
9. Srinivasan R, Xu L, Spicer RL, Tungate FL, Davis BH (1996) Fuel Sci Technol Int 14(10):1337
10. Davis BH (1999) Technology development for iron Fischer–Tropsch Catalysis, US DOE Final Technical Report, Contract # DE-AC22-94PC94055-13
11. Kuo JCW, Sanzo FPD, Garwood WE, Gupte KM, Lang CK, Leib TM, Malladi M, Molina T, Nace DM, Smith J, Tarallo N, Kirk JF (1983) Slurry Fischer–Tropsch/Mobil two-stage process of converting syngas to high octane gasoline, US DOE Final Technical Report, Contract # AC22-80PC30022
12. Bukur DB, Ma WP, Vazquez VC, Nowicki L, Adeyiga AA (2004) Ind Eng Chem Res 43:1359
13. O'Brien RJ, Xu L, Bao S, Raje A, Davis BH (2000) Appl Catal A 196:173
14. Kölbel H, Ralek M (1980) Catal Rev-Sci Eng 21:225
15. Niemantsverdriet JW, van der Krann AM, van Dijk WL, van der Baan HS (1980) J Phys Chem 84:3363
16. Butt JB (1990) Catal Lett 7:61
17. Sarkar A, Dozier AK, Graham UM, Thomas G, O'Brien RJ, Davis BH (2007) Appl Catal A: Gen 326:55
18. Rao KRPM, Huggins FE, Huffman GP, Gormley RJ, O'Brien RJ, Davis BH (1996) Energy Fuels 10:546
19. Rao KRPM, Huggins FE, Huffman GP, O'Brien RJ, Gormley RJ, Davis BH (1995) ACS Division Fuel Chem 40(1):153 (Preprints of Papers)
20. Jin Y, Xu H, Datye AK (2006) Microsc Microanal 12:124
21. Cullity BD, Stock SR (2001) Elements of X-ray diffraction, 3rd edn. Prentice Hall, Upper Saddle River, NJ, USA, p 118, 182
22. Morozova OS, Maksimov YV, Shashkin DP, Shirjaev PA, Matveyev VV, Zhorin VA, Krylov OV (1991) Appl Catal 78:227
23. PDF # 19-0629, JCPDS—International Center for Diffraction Data (2003)
24. PDF # 36-1248, JCPDS—International Center for Diffraction Data (2003)
25. Colliex C, Manoubi T, Ortiz C (1991) Phys Rev B 44(20):402
26. Allen T (1997) Particle size measurement, vol 1. Chapman and Hall, London, p 44
27. Dry ME (1981) In: Anderson JR, Boudart M (eds) Catalysis-science and technology. Springer-Verlag, New York, p 59
28. Emmett PH (ed) (1956) Crystallite phase and their relationship to Fischer–Tropsch catalysis. Reinhold, New York, p 407
29. Zarochak MF, McDonald MA (1986) Slurry-phase Fischer–Tropsch synthesis, CONF-86/288-1, Proceedings of Indirect Liquefaction Contractor's Conference, December 2–4, 1986 at Monroeville, PA, USA
30. Raupp GB, Delgass WN (1979) J Catal 58:361
31. Li S, O'Brien RJ, Meitzner GD, Hamdeh H, Davis BH, Iglesia E (2001) Appl Catal A 219:215
32. Li S, Meitzner GD, Iglesia E (2001) J Phys Chem B 105:5743
33. Xu J, Bartholomew CH (2005) J Phys Chem B 109:2392
34. Loaiza-Gil A, Fontal B, Rueda F, Mendialdua J, Casanova R (1999) Appl Catal A: Gen 177:193
35. Eliason SA, Bartholomew CH (1997) Stud Surf Sci Catal 111:517
36. Dwyer DJ, Hardenbergh JH (1984) J Catal 87:66
37. Jin Y, Datye AK (2000) J Catal 196:8
38. Fernández A, Prieto P, Quirós C, Sanz JM, Martin JM, Vacher B (1996) Appl Phys Lett 69:764
39. Kim WJ, Ruano OA, Wolfenstine J, Frommeyer G, Sherby OD (1997) J Mater Res 12:2317